A secondary zone of uplift measured after megathrust earthquakes: caused by early downdip afterslip?

Théa Ragon[1] and Mark Simons[1]

[1]Caltech

November 24, 2022

Abstract

A secondary zone of surface uplift (SZU), located ~300 kilometers from the trench, has been measured after several megathrust earthquakes. The SZU reached a few centimeters hours after the 2011 Mw 9.1 Tohoku (Japan) earthquake. Less than a day after the 2010 Mw 8.8 Maule (Chile) earthquake, it peaked at 12 cm. Published coseismic finite-fault models for these events do not reproduce the measured SZU.

One interpretation is that this SZU is universal, driven by volume deformation around the slab interface (van Dinther et al. 2019). In contrast, with synthetic tests and an investigation of the Maule event, we demonstrate the SZU may instead result from slip on the slab interface. Further, we suggest that slip occurs as rapid postseismic afterslip. We can reproduce the SZU with fault slip if elastic heterogeneities associated with the subducting slab are accounted for, as opposed to assuming homogeneous or layered elastic lithospheric structures.

A secondary zone of uplift measured after megathrust earthquakes: caused by early downdip afterslip?

Théa Ragon[1], **Mark Simons**[1]

[1]Seismological Laboratory, California Institute of Technology, Pasadena, CA, USA.

Key Points:

- After large subduction earthquakes, a secondary zone of uplift (SZU) is measured in the forearc several hundred kilometers from the trench
- The SZU is not reproduced by coseismic finite-fault models that neglect 3D elastic heterogeneities in lithospheric structure
- The SZU is reproduced using plausible models of 3D elastic heterogeneities, and is likely due to slip down-dip of the main coseismic patch

Corresponding author: Théa Ragon, `tragon@caltech.edu`

Abstract

A secondary zone of surface uplift (SZU), located ∼300 kilometers from the trench, has been measured after several megathrust earthquakes. The SZU reached a few centimeters hours after the 2011 M_w 9.1 Tohoku (Japan) earthquake. Less than a day after the 2010 M_w 8.8 Maule (Chile) earthquake, it peaked at 12 cm. Published coseismic finite-fault models for these events do not reproduce the measured SZU. One interpretation is that this SZU is universal, driven by volume deformation around the slab interface (van Dinther et al. 2019). In contrast, with synthetic tests and an investigation of the Maule event, we demonstrate the SZU may instead result from slip on the slab interface. Further, we suggest that slip occurs as rapid postseismic afterslip. We can reproduce the SZU with fault slip if elastic heterogeneities associated with the subducting slab are accounted for, as opposed to assuming homogeneous or layered elastic lithospheric structures.

Plain Language Summary

Large earthquakes in subduction zones induce displacement of the ground surface, which usually include large amplitude uplift close to the shore, and a mild region of subsidence further inland. After the largest instrumented earthquakes, such as the 2011 M_w 9.1 Tohoku (Japan), the 1960 M_w 9.5 Valdivia (Chile) and 1964 M_w 9.2 Alaska earthquakes, a secondary zone of uplift (SZU) is detectable even further inland. The origin of this SZU remains enigmatic, but one interpretation is that it derives from deformation of the volume around the subducting fault (van Dinther et al. 2019). In this study, we investigate potential interpretations of its origin, including simple afterslip models. A simple slip model with realistic variations in crustal elastic properties allows one to reproduce the secondary zone of uplift. We then focus on the 2010 M_w 8.8 Maule (Chile) event, for which secondary uplift peaked at 12 cm. Unlike previously published studies, we can reproduce the SZU with aseismic on-fault displacement, located significantly deeper than the region of estimated coseismic slip. This deeper slip likely occurred in the hours to days after the earthquake.

1 Introduction

Models of subduction zone thrust earthquakes based on a dip-slip dislocation embedded in an elastic half space produce a large surface uplift in near field, and a zone of small amplitude subsidence that slowly tapers to zero in the far field (Fig. 1a, primary slip patch, e.g., Savage, 1983). Vertical displacements measured after most subduction earthquakes follow a similar pattern. However, far field geodetic measurements of megathrusts earthquakes (M_w >8) detect a secondary zone of uplift (refer to as SZU in the text) a few hundred kilometers from the trench (for a summary, see van Dinther et al., 2019). In the years following the 1960 M_w 9.5 Valdivia and 1964 M_w 9.2 Alaska earthquakes (e.g., Plafker & Savage, 1970; Kanamori, 1970), uplift of more than 1 m and 30 cm in amplitude, respectively, were measured in this secondary zone. The 2010 M_w 8.8 Maule and 2011 M_w 9.0 Tohoku earthquakes each produced a few centimeters of secondary uplift in the few hours to days following the mainshock (Figs 1c, S1, as measured by GNSS, Vigny et al., 2011; Ozawa et al., 2011). Whether this uplift is coseismic or rapid postseismic is unknown at this time.

The origin and consistency of the SZU remains ambiguous. None of the published coseismic slip models of the 2010 Maule event reproduce the horizontal deformation, the near-field vertical displacements and the SZU (Fig. 1c and enclosed references, Vigny et al., 2011). Similarly, none of the published coseismic slip models for the 2011 Tohoku earthquake explain the observed SZU, whose amplitude is less than a twentieth of the near-field vertical displacement. Note that, for these two events, long-term postseismic SZU can be modeled with afterslip or viscoelastic processes (e.g.,

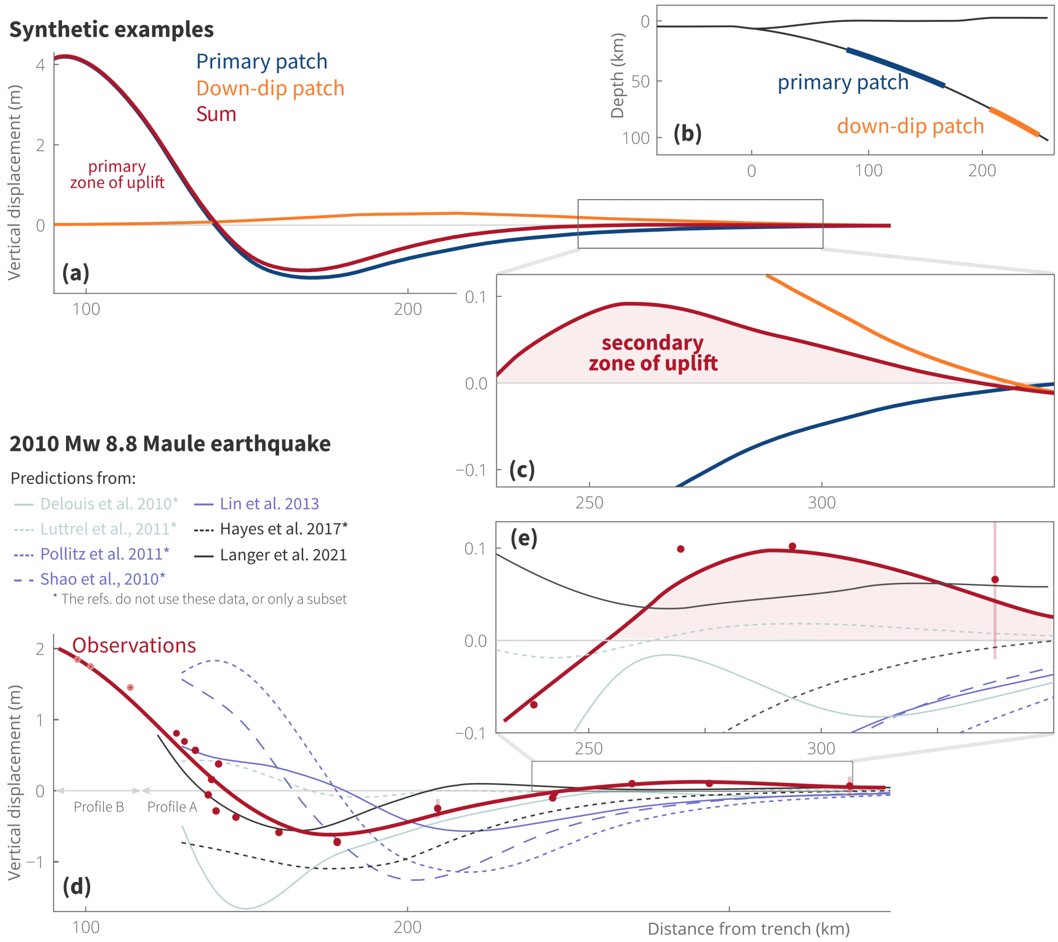

Figure 1. Synthetic and observed trench perpendicular profiles of vertical surface displacements. (a) Vertical surface displacement induced by a ∼40-km-deep primary slip patch, by a secondary down-dip patch (∼ 90-km-depth), and the sum of the two. The zoomed inset (c) shows that the sum of these two patches induces a ∼10 cm secondary zone of uplift ∼250 km from the trench. (b) Cross section of the synthetic subduction zone, with the location of the primary and down-dip slip patches. (c) Measured and predicted vertical surface displacements for the 2010 M_w 8.8 Maule earthquake for profile A (location in Figs S1 and 5). The zoomed inset shows the inability of published finite fault slip models to explain the secondary zone of uplift. Slip models from Delouis et al. (2010); Luttrell et al. (2011); Pollitz et al. (2011); Lin et al. (2013); Hayes (2017); Langer et al. (2020) have been retrieved from the SRCMOD database (Mai & Thingbaijam, 2014); note that these models were derived using different datasets (not necessarily the data shown here). Location of the profile, data and other trench-perpendicular profiles shown in Fig. S1. Vertical bars indicate measurement errors when available.

Klein et al., 2016; Ichimura et al., 2016; Li et al., 2017; Agata et al., 2019; Peña et al., 2020). But classic elastic or viscoelastic rebound models fail to predict any coseismic SZU (van Dinther et al., 2019). van Dinther et al. (2019) propose that the SZU is universal, coseismic, and that is is the result of an elastic rebound of the lithosphere and an upward elastic flow in the mantle wedge.

While a single patch of fault slip cannot produce a SZU at the surface, an additional down-dip patch potentially can (Fig. 1a). We should expect that a finite-fault model could infer a down-dip slip patch to explain any observed SZU. However, existing published slip models do not.

In the following, we investigate under which assumptions this secondary zone of uplift can, or cannot, be predicted with fault slip. We focus on the Maule event, where SZU could not be reproduced (Fig 1c) even with added complexity in crustal properties: curved and deeper slab geometries, topography, heterogeneous crustal elastic properties, etc (Lin et al., 2013; Moreno et al., 2012; Langer et al., 2020); but where the particular effect of a stiffer subducting slab, and more compliant forearc, has not been included. While we do not discard the possibility that the secondary zone of uplift might be affected by deformation of the volume around the slab interface, we show it may simply be the result of slip on this interface. We first investigate the effect of 3D elastic heterogeneities for a synthetic case and apply this model to an analysis of the Maule earthquake. We conclude with a discussion of the timing of the SZU relative to the mainshock.

2 A synthetic example: secondary zone of uplift caused by down-dip slip

We begin by designing a synthetic subduction zone, where the lithosphere is divided in domains of different elastic properties, generic trench-perpendicular topographic variations and a curved slab interface whose architecture varies slightly along strike (Fig. 2f). This subduction zone is characterized by a stiff plunging slab overlain by a compliant oceanic crust; the continental domain consists of a 35-km-thick crust, more compliant than the underlying mantle whose density increases with depth (domain properties detailed in Suppl. Mat. Text S2, Tab. S1, Figs S2, S3). We apply slip on a limited region of the slab interface (Fig. 1b). Because of the inhomogeneous elastic structure, we rely on a finite element approach (Pylith, Aagaard et al., 2013) to calculate surface displacements.

We first compare the strain produced by a ∼40-km-deep slip patch on the assumed fault, embedded either in a 3D lithosphere or in a layered crust (Fig. 2). The layered crust replicates the continental domain of its 3D counterpart and does not incorporate variations in topography (Fig. 2g). Relative to the layered elastic models, the 3D-heterogeneous models produce a primary zone of subsidence (150-200 km from the trench) that is smaller in amplitude and tapers to zero closer to the trench. In the region of primary subsidence, the impact of elastic heterogeneity is ∼5 times larger for vertical displacements than for horizontal ones (Figs 2, S4, 25% of peak amplitude versus 5% respectively).

We then assume two slip patches, the primary patch peaks at 17 m of slip while the secondary down-dip patch has 3.5 m of slip (Fig. 1b). With the heterogeneous elastic model, we calculate the induced displacement at 50 locations randomly distributed at the surface, along with two additional E-W profiles; these locations imitate the spatial distribution of the GNSS data of the Maule event (Fig S1, Vigny et al., 2011). Induced displacements reproduce the ∼15-cm-uplift measured 250-300 km away from the trench after the Maule earthquake (Figs 1a and d, S1). We add white and spatially correlated noise to these synthetic data, and try to recover the target slip patches as-

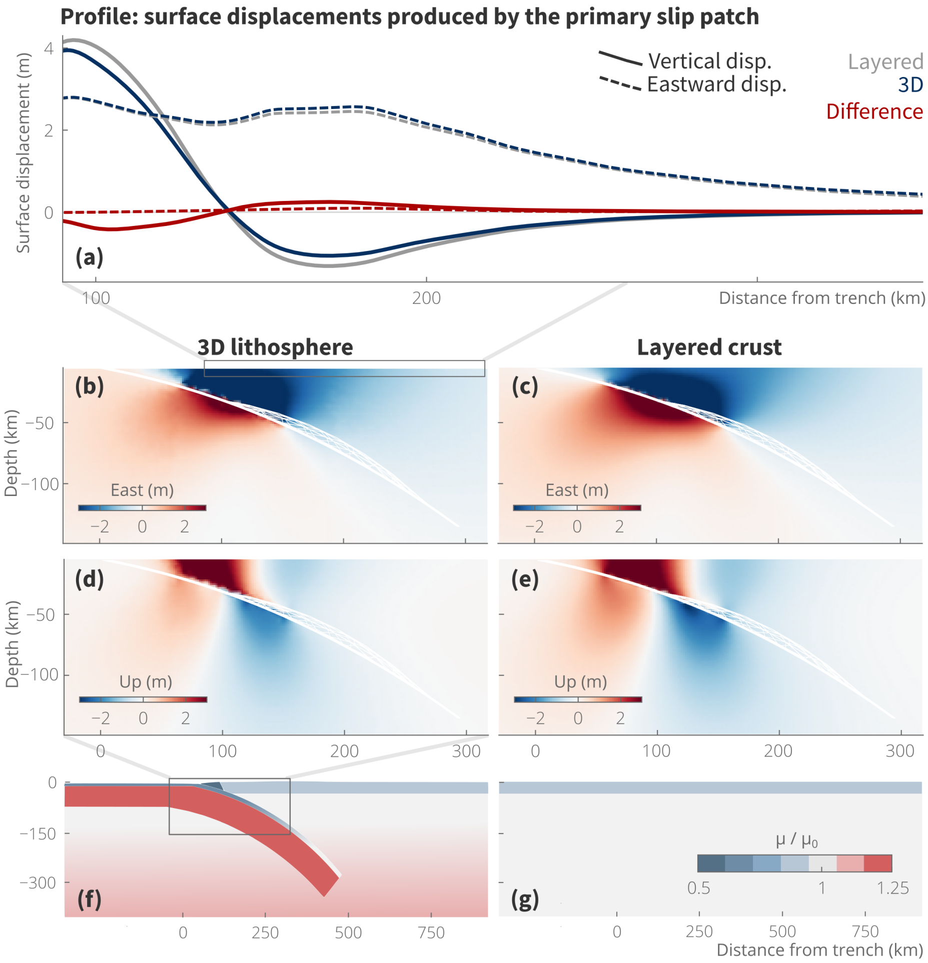

Figure 2. Displacements produced by a ∼40-km-deep slip patch on a slab embedded in a 3D lithosphere or a layered crust. (a) Trench-perpendicular profiles of surface displacements. (b,d) and (c,e) Trench-perpendicular cross-sections of upward and eastward displacements for the elastic properties shown in (f) and (g), respectively.

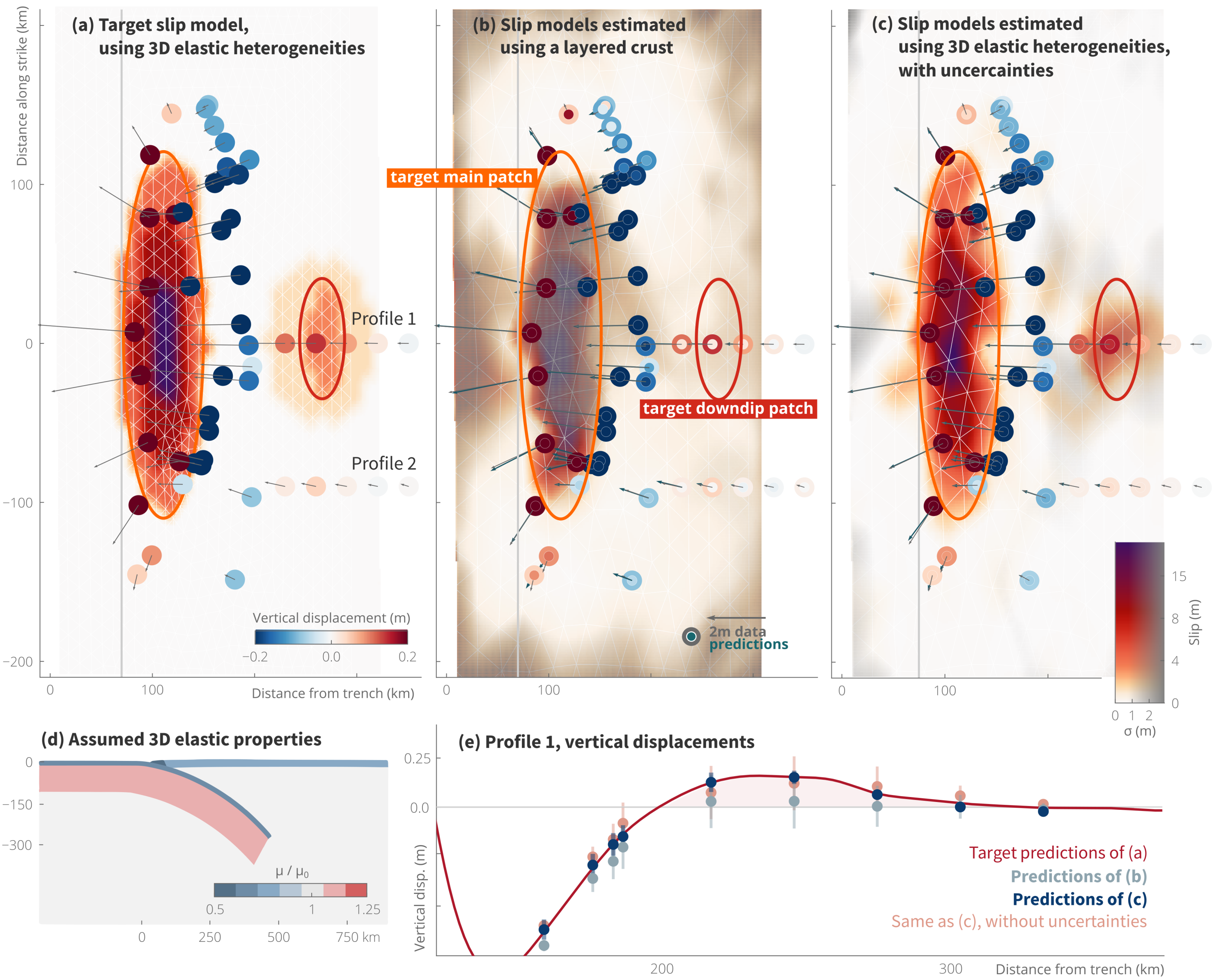

Figure 3. Synthetic example: (a) Target slip and surface displacements. (b,c) Inferred slip and surface displacement assuming incorrect lithospheric structure, either with a layered crust (b) or with 3D-varying elastic properties, shown in (d). Gray shading is the standard deviation of the inferred slip. In (b) and (c), the assumed fault replicates the true geometry shown in (a), but extends to greater depths. In (c), uncertainties in elastic properties are accounted for: Note the difference in the spatial distribution of posterior uncertainties. (d) Assumed 3D elastic properties, μ_0=52 GPa, which differ from the properties used to calculate synthetic observations (displayed in Fig. 2f). (e) Trench perpendicular profile of the target synthetic data and predicted vertical displacements (at 0-km-along-strike). Vertical error bars indicate the posterior uncertainty. Predictions in light red are for the model shown in Fig. S8.

suming the correct fault geometry (with larger subfaults) and a layered elastic structure (layered as in Fig. 2g, or inexact material properties with 3D variations, Fig. 3d). We use a Bayesian sampling approach to infer fault slip from the synthetic displacement (detailed in Suppl. Mat. section S1, Minson et al., 2013).

When the crust is assumed layered (or homogeneous), the secondary uplift cannot be fit (and is not within posterior uncertainty, Fig. 3a,c, Fig. S5, respectively). Relative to the model with heterogeneous elastic properties, a layered crust produces wider and larger primary zone of subsidence, while the horizontal displacements are only slightly impacted (Fig. 2). The amount of slip required to explain the horizontal displacements is incompatible with the slip required to explain the vertical ones. Most inversions typically favor fitting the horizontal measurements, since they are larger and usually more certain. Some down-dip slip is imaged, as required by the horizontal displacements, if the fault is deep enough. Assuming a fault model that is too shallow, and/or subject to unphysical spatial smoothing, can prevent resolution of the down-dip patch (Fig. S6). The SZU can be produced with incorrect inferred slip, and to the detriment of the fit to the horizontal displacements, if assuming very low measurement errors for the vertical displacements only (1 mm, i.e. very strongly favoring their fit) and a fault geometry that extends to great depths (Fig. S7).

In contrast, adopting a relatively realistic crustal structure (e.g., with 3D heterogeneities in elastic properties for a typical subduction zone, even if the properties are imperfectly known, detailed in Tab. S2), allows one to reproduce the SZU, and to recover the down-dip slip patch (Fig. 3b,c). Accounting for uncertainties in elastic properties (following the methodology presented in Ragon & Simons, 2021, Fig. 3c,d) improves the fit to the data. The main annoyance in assuming heterogeneous crustal elastic properties for slip inference is the computational burden. With this simple synthetic example, we show that a SZU can be produced by down-dip slip on the slab interface by accounting for 3D variations in elastic properties.

3 The 2010 M_w 8.8 Maule earthquake: Ockham's Razor for secondary uplift

The results of our synthetic example suggest that assuming a realistic crustal structure when imaging the coseismic slip of the Maule event may allow one to reproduce the measured SZU. To this end, we build a realistic crustal model for the calculation of the Green's functions (Figs S9, S10, slab geometry from Slab2, elastic properties from LITHO1.0, topography from ETOPO1, Hayes et al., 2018; Pasyanos et al., 2014; NCEI, 2008). While more detailed models might be available, our goal is to explore the secondary uplift, not to image the slip in detail. We also account for potential uncertainties in the assumed fault geometry and elastic properties (following the methodology presented in Ragon & Simons, 2021). We solve for the slip distribution and amplitude using the GNSS data from Lin et al. (2013).

The inferred slip model reproduces the SZU (Fig. 4). We image a primary zone of fault slip below the coastal region, with a relatively large uncertainty due to the limited amount of data considered here. Down-dip of this primary region of slip, we infer a well-constrained slip zone with an amplitude of 2.5-3 m, equivalent to M_w=7.2, which is responsible for the secondary uplift. Models assuming a layered or homogeneous crust do not image this down-dip slip and do not reproduce the SZU (Fig. 1c and enclosed references, Figs S11, S12, S13). Models assuming an inexact heterogeneous elastic structure, but neglecting related epistemic uncertainties, are able to reproduce the SZU albeit not as well as when epistemic uncertainties are accounted for (Figs S12, S13).

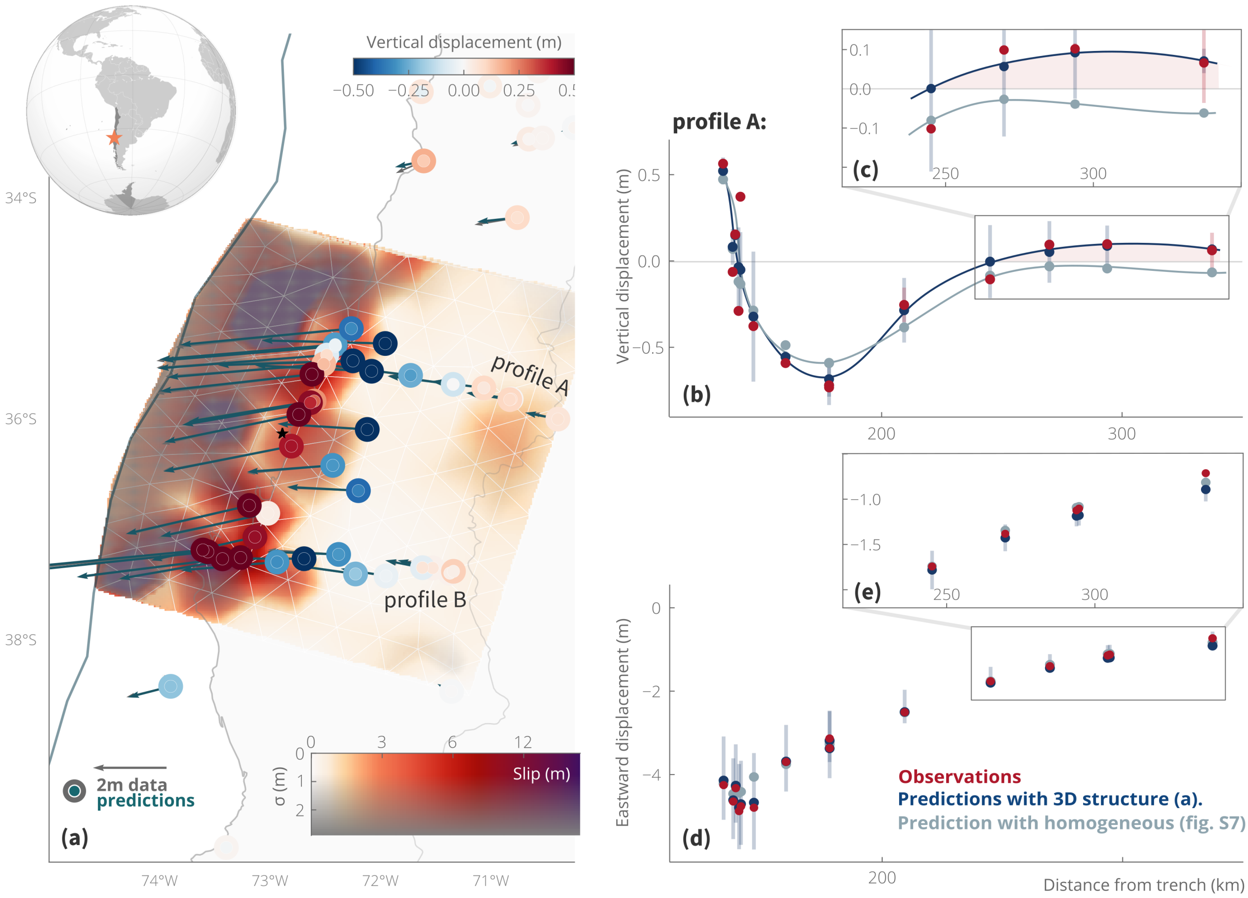

Figure 4. The 2010 M_w 8.8 Maule earthquake: (a) inferred coseismic slip model as well as observed and predicted surface displacements, assuming a 3D crustal structure and accounting for related epistemic uncertainties. Grey shading indicates the standard deviation of the inferred slip. (b) Trench perpendicular profile (profile A) of measured and predicted vertical displacements, for the slip model shown in (a), and a slip model inferred assuming an homogeneous crustal structure (Fig. S10). Vertical error bars indicate the posterior uncertainty and data errors. (d) Same as (b) for eastward surface displacements. (c) and (e) Zoomed inset on the SZU region.

Our results suggest that previously published models for the Maule earthquake were not able to reproduce the SZU (Fig. 1c) because most of them were inferred assuming a layered crust. While Moreno et al. (2012) assumed 3D heterogeneous elastic properties, the shallow fault geometry they used and the impact of spatial regularization likely prevented a down-dip patch to be imaged. Note that some authors infer a down-dip patch, as required by horizontal displacements, that could not be associated with the SZU for the same reasons (as shown in our synthetic example, Fig. 3a, Vigny et al., 2011; Bedford et al., 2013). The combined effect of strong assumptions on the crustal elastic structure and fault geometry, and the common use of unphysical regularization (e.g., Ortega-Culaciati et al., 2021), probably prevented most published models from producing the mild secondary uplift of the Tohoku earthquake.

That we image down-dip slip does not mean slip is uniquely the cause of the SZU. What we know is that the responsible mechanism should occur very early after the mainshock, at most a few hours to days (as measured by GNSS). Hence, the model proposed by Luo and Wang (2021), which requires a ∼5-years-long postseismic visco-elastic relaxation to produce the SZU, is too slow to explain these observations. Similarly, challenges in modeling highly disparate time-scales (from seconds to years) prevent van Dinther et al. (2019) from confirming the universal process they invoke is coseismic, rather than lasting several weeks after the mainshock. In contrast, while the potential influence of volume deformation cannot be ruled out, the hypothesis that down-dip slip caused the SZU seems straightforward.

4 Is the secondary zone of uplift induced by down-dip rapid afterslip?

For the Maule earthquake, we infer down-dip slip at ∼90-km-depth, where only a few aftershocks occurred, none with $M_w > 6$ (Rietbrock et al., 2012; Lange et al., 2012). Such depths are generally believed to be relatively aseismic (Lay et al., 2012; Obara & Kato, 2016). Moreover, in south-central Chile intermediate-depth seismicity is relatively sparse (Fig. 5 Ruiz & Madariaga, 2018) We conclude that the down-dip slip we image (equivalent M_w=7.2) is likely aseismic in nature, and therefore postseismic. To confirm this hypothesis, we estimate the postseismic deformation that affected the slab interface in the days to months following the mainshock, using similar modeling assumptions to the coseismic case and GNSS observations. Again, our goal here is not to accurately model the postseismic slip. Rather, we wish to verify if afterslip at the location of the down-dip patch we image could be consistent with measured postseismic surface displacements. Due to the limited number of postseismic observations, many slip models are plausible and our stochastic results are poorly informative. We thus rely on a two-steps approach. We first verify if deep slip is within the estimated range of plausible parameters (i.e., within the posterior marginal probability density functions). Then, we specifically check if deep afterslip is coherent with available measurements. To do so, we build a synthetic afterslip model that consists of the previously estimated mean afterslip at depths shallower than 70 km, with additional synthetic slip at ∼90-km-depth, and compare produced surface displacements with available data.

We first model the first 12 days of afterslip: only 3 GNSS stations are located above the fault (data from Vigny et al., 2011, the vertical component is too noisy to be used). Larger westward displacements above the deepest portion of the fault suggest deep afterslip occurred, even if its location is not constrained. Synthetic afterslip at the location of the down-dip patch, added to the estimated 12-days-afterslip model, is coherent with the few available measurements (Figs 5, S14). We also model the postseismic slip in the year following the mainshock (few vertical measurements are available, data spanning 488 days after the rupture, from Lin et al., 2013). While slip at the exact location of the down-dip patch does not appear in the posterior mean model (Fig. S15a), it is within plausible values (Fig. S15c). A synthetic ∼1-m-amplitude

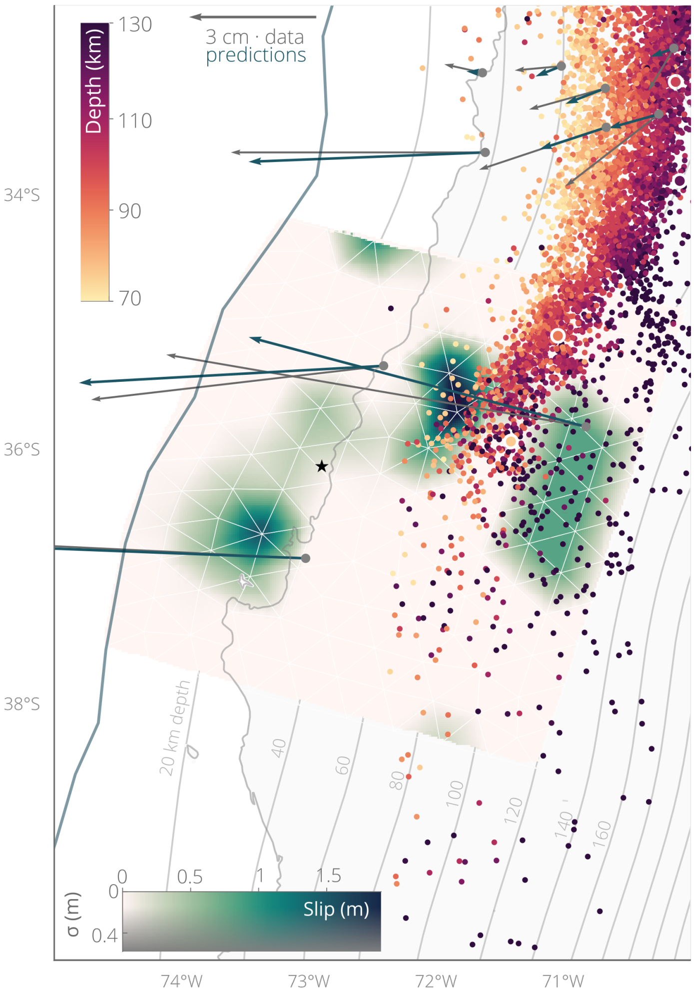

Figure 5. Early afterslip (12 days) following the 2010 M_w 8.8 Maule earthquake, inferred from available GNSS horizontal displacements (published data σ of less than 4 mm Vigny et al., 2011) and with additional synthetic downdip afterslip. Overlayed is the recent seismicity, including aftershocks of the Maule event, that have occurred between 70 and 130-km-depth, from the USGS ANSS Comprehensive Earthquake Catalog (ComCat, events since 1928, $M_w > 3$). Earthquakes with $M_w > 6$ are indicated as large points with a white edge. Slab-depth contours in light gray are from Slab2; they are not in perfect agreement with seismicity depth.

down-dip slip patch is consistent with distal observations (Fig. S15b). Further, the vertical component of distal data requires deep slip (Fig. S15) but is not sensitive to its exact location.

Other authors infer similar deep postseismic slip (60- to 90-km-depth, Vigny et al., 2011; Lin et al., 2013; Bedford et al., 2013). However, we note that at such timescales, more than 1 year after the mainshock, viscoelastic relaxation also could reproduce the measured displacements (as demonstrated by Klein et al., 2016; Peña et al., 2020, 2021), and that we cannot discriminate between postseismic slip or viscoelastic relaxation. The down-dip slip we image is therefore consistent with surface displacements measured 12-days and >1 year after the coseismic rupture, further suggesting the SZU has possibly been caused by very rapid afterslip, which then could have slipped continuously in the days to months following the coseismic rupture.

5 Discussion and conclusion

A secondary zone of uplift (SZU) has been observed after several megathrust earthquakes. The SZU reached more than 12 cm following the 2010 M_w 8.8 Maule (southern Chile) earthquake. In this study, we investigate if (and which) assumptions in the foward and/or inverse approach could prevent the SZU to be reproduced with slip on the slab interface. We show that neglecting variations in elastic properties due to the plunging slab induces an incompatibility in the amount of slip required to explain the measured horizontal, or vertical, displacements, preventing models from reproducing the SZU. In contrast, we demonstrate that assuming realistic heterogeneous elastic properties, a sufficiently deep fault geometry, and discarding any non-physical regularization of the inverse problem, we infer the SZU as caused by slip down-dip of the main coseismic rupture.

Our synthetic tests suggest that assuming plausible, but inexact, 3D-heterogeneous elastic properties is sufficient to recover the SZU. Accounting for potential uncertainties in these properties (Ragon & Simons, 2021) allows us to improve the fit to the observations, and to decrease posterior uncertainty on slip amplitude and surface displacement predictions. Accounting for epistemic uncertainties usually produce opposite effects, increasing posterior uncertainties and residuals (Ragon et al., 2018, 2019). In this particular case, we believe introducing uncertainties in the elastic structure promotes the exploration of a narrow region of the solution space that is otherwise not within reach.

For the Maule earthquake, we show that slip down-dip of the coseismic rupture ($\sim$90-km-depth) produces a SZU, and that this slip is likely postseismic in nature. Deep afterslip or slow slip events have been observed along the Peru-Chile trench, in northern Chile (M_w 6.9, 50-km-depth, Klein et al., 2018) or Ecuador (before and after the 2016 M_w 7.8 Pedernales earthquake, $\sim$60-km-depth, Rolandone et al., 2018; Tsang et al., 2019). However, the slab geometry and seismicity distribution in the Maule region clearly differ from northern South-America (Fig. 5), preventing further comparisons. In particular, the down-dip slip would have occurred at the transition between the flat slab of central Chile to a more moderately dipping slab in south Chile, as indicated by recent seismicity (Fig. 5, Pesicek et al., 2012).

Klein et al. (2018) report an inconsistency in the amount of slow slip needed to fit horizontal versus vertical observations a few hundreds of km from the trench. Both postseismic slip models of the Maule event (Lin et al., 2013), and synthetic tests performed for an infinitely long megathrust (Hsu et al., 2006), report similar inconsistencies in the fit to vertical versus horizontal measurements. It is common practice to discard or down-weight vertical data because of such inconsistencies and larger measurement errors. We show that by accounting for heterogeneities in elastic structure, we can reconcile vertical and horizontal observations.

The SZU observed after megathrust earthquakes other than the Maule event is located 300 km from the trench in Chile, 350 km in Japan, and 400 km in Alaska (van Dinther et al., 2019). Assuming that the SZU finds its origin in slip down-dip of the coseismic rupture, because of the various slab geometries, the down-dip slip would have consistently occurred at ∼80-90-km-depth. Due to the lack of observations (in Japan, a potential down-dip slip would be observed mostly offshore), we cannot discriminate whether the secondary zone uplift is systematically caused by fault slip or other processes.

Acknowledgments
MS was partially supported by the National Aeronautics and Space Administration under Grant No. 80NSSC19K1499. We thank Rishav Mallick for fruitful discussions.

Data availability statement. Materials presented in this paper are archived and available in Ragon (2022). The Bayesian simulations were performed with the AlTar2 package (*AlTar, A Bayesian Framework for Inverse Problems*, 2022). The Classic Slip Inversion (CSI) Python library (Jolivet et al., 2014) developed by Romain Jolivet was used to build inputs for the Bayesian algorithm. The mesh for the FEM simulations was built using Coreform Cubit (*Coreform Cubit*, 2022). We used the finite-element code Pylith (Aagaard et al., 2013) to perform the simulations. GNSS data have been published in Vigny et al. (2011) and Lin et al. (2013). Slab geometry, topography and crustal elastic properties from Slab2, LITHO1.0, and ETOPO1 models are available in Hayes et al. (2018); Pasyanos et al. (2014); NCEI (2008). 3D data were visualized using the open-source parallel visualization software ParaView/VTK (Ahrens et al., 2005). Figures were generated with the Matplotlib (Hunter, 2007) and Seaborn (Waskom, 2021) Python3 libraries.

References

Aagaard, B. T., Knepley, M. G., & Williams, C. A. (2013). A domain decomposition approach to implementing fault slip in finite-element models of quasi-static and dynamic crustal deformation. *Journal of Geophysical Research: Solid Earth*, *118*(6), 3059–3079. doi: 10.1002/jgrb.50217

Agata, R., Barbot, S. D., Fujita, K., Hyodo, M., Iinuma, T., Nakata, R., ... Hori, T. (2019). Rapid mantle flow with power-law creep explains deformation after the 2011 Tohoku mega-quake. *Nature Communications*, *10*(1), 1385. doi: 10.1038/s41467-019-08984-7

Ahrens, J., Geveci, B., & Law, C. (2005). 36 - ParaView: An End-User Tool for Large-Data Visualization. In C. D. Hansen & C. R. Johnson (Eds.), *Visualization Handbook* (pp. 717–731). Burlington: Butterworth-Heinemann. doi: 10.1016/B978-012387582-2/50038-1

AlTar, A Bayesian framework for inverse problems. (2022). v2.0, ParaSim Inc., California Institute of Technology. Available at github.com/lijun99/altar2-documentation.

Bedford, J., Moreno, M., Baez, J. C., Lange, D., Tilmann, F., Rosenau, M., ... Vigny, C. (2013). A high-resolution, time-variable afterslip model for the 2010 Maule Mw = 8.8, Chile megathrust earthquake. *Earth and Planetary Science Letters*, *383*, 26–36. doi: 10.1016/j.epsl.2013.09.020

Coreform Cubit. (2022). v2022.4. Orem, UT: Coreform LLC. Retrieved from coreform.com.

Delouis, B., Nocquet, J.-M., & Vallée, M. (2010). Slip distribution of the February 27, 2010 Mw = 8.8 Maule Earthquake, central Chile, from static and high-rate

GPS, InSAR, and broadband teleseismic data. *Geophysical Research Letters*, *37*(17). doi: 10.1029/2010GL043899

Hayes, G. P. (2017). The finite, kinematic rupture properties of great-sized earthquakes since 1990. *Earth and Planetary Science Letters*, *468*, 94–100. doi: 10.1016/j.epsl.2017.04.003

Hayes, G. P., Moore, G. L., Portner, D. E., Hearne, M., Flamme, H., Furtney, M., & Smoczyk, G. M. (2018). Slab2, a comprehensive subduction zone geometry model. *Science*, *362*(6410), 58–61. doi: 10.1126/science.aat4723

Hsu, Y.-J., Simons, M., Avouac, J.-P., Galetzka, J., Sieh, K., Chlieh, M., … Bock, Y. (2006). Frictional Afterslip Following the 2005 Nias-Simeulue Earthquake, Sumatra. *Science*, *312*(5782), 1921–1926. doi: 10.1126/science.1126960

Hunter, J. D. (2007). Matplotlib: A 2D Graphics Environment. *Computing in Science & Engineering*, *9*(3), 90–95. doi: 10.1109/MCSE.2007.55

Ichimura, T., Agata, R., Hori, T., Hirahara, K., Hashimoto, C., Hori, M., & Fukahata, Y. (2016). An elastic/viscoelastic finite element analysis method for crustal deformation using a 3-D island-scale high-fidelity model. *Geophysical Journal International*, *206*(1), 114–129. doi: 10.1093/gji/ggw123

Jolivet, R., Duputel, Z., Riel, B., Simons, M., Rivera, L., Minson, S. E., … Fielding, E. J. (2014). The 2013 Mw 7.7 Balochistan Earthquake: Seismic Potential of an Accretionary Wedge. *Bulletin of the Seismological Society of America*, *104*(2), 1020–1030. doi: 10.1785/0120130313

Kanamori, H. (1970). The Alaska Earthquake of 1964: Radiation of long-period surface waves and source mechanism. *Journal of Geophysical Research (1896-1977)*, *75*(26), 5029–5040. doi: 10.1029/JB075i026p05029

Klein, E., Duputel, Z., Zigone, D., Vigny, C., Boy, J.-P., Doubre, C., & Meneses, G. (2018). Deep Transient Slow Slip Detected by Survey GPS in the Region of Atacama, Chile. *Geophysical Research Letters*, *45*(22), 12,263–12,273. doi: 10.1029/2018GL080613

Klein, E., Fleitout, L., Vigny, C., & Garaud, J. (2016). Afterslip and viscoelastic relaxation model inferred from the large-scale post-seismic deformation following the 2010 Mw 8.8 Maule earthquake (Chile). *Geophysical Journal International*, *205*(3), 1455–1472. doi: 10.1093/gji/ggw086

Lange, D., Tilmann, F., Barrientos, S. E., Contreras-Reyes, E., Methe, P., Moreno, M., … Beck, S. (2012). Aftershock seismicity of the 27 February 2010 Mw 8.8 Maule earthquake rupture zone. *Earth and Planetary Science Letters*, *317-318*, 413–425. doi: 10.1016/j.epsl.2011.11.034

Langer, L., Ragon, T., Sladen, A., & Tromp, J. (2020). Impact of topography on earthquake static slip estimates. *Tectonophysics*, 228566. doi: 10.1016/j.tecto.2020.228566

Lay, T., Kanamori, H., Ammon, C. J., Koper, K. D., Hutko, A. R., Ye, L., … Rushing, T. M. (2012). Depth-varying rupture properties of subduction zone megathrust faults. *Journal of Geophysical Research: Solid Earth*, *117*(B4). doi: 10.1029/2011JB009133

Li, S., Moreno, M., Bedford, J., Rosenau, M., Heidbach, O., Melnick, D., & Oncken, O. (2017). Postseismic uplift of the Andes following the 2010 Maule earthquake: Implications for mantle rheology. *Geophysical Research Letters*, 2016GL071995. doi: 10.1002/2016GL071995

Lin, Y.-n. N., Sladen, A., Ortega-Culaciati, F., Simons, M., Avouac, J.-P., Fielding, E. J., … Socquet, A. (2013). Coseismic and postseismic slip associated with the 2010 Maule Earthquake, Chile: Characterizing the Arauco Peninsula barrier effect. *Journal of Geophysical Research: Solid Earth*, *118*(6), 3142–3159. doi: 10.1002/jgrb.50207

Luo, H., & Wang, K. (2021). Postseismic geodetic signature of cold forearc mantle in subduction zones. *Nature Geoscience*, *14*(2), 104–109. doi: 10.1038/s41561-020-00679-9

Luttrell, K., Tong, X., Sandwell, D., Brooks, B., & Bevis, M. (2011). Estimates of stress drop and crustal tectonic stress from the 27 February 2010 Maule, Chile, earthquake: Implications for fault strength [Journal Article]. *Journal of Geophysical Research B: Solid Earth*, *116*(11). doi: 10.1029/2011JB008509

Mai, P. M., & Thingbaijam, K. K. S. (2014). SRCMOD: An Online Database of Finite-Fault Rupture Models. *Seismological Research Letters*, *85*(6), 1348–1357. doi: 10.1785/0220140077

Minson, S. E., Simons, M., & Beck, J. L. (2013). Bayesian inversion for finite fault earthquake source models I – theory and algorithm. *Geophysical Journal International*, *194*(3), 1701–1726. doi: 10.1093/gji/ggt180

Moreno, M., Melnick, D., Rosenau, M., Baez, J., Klotz, J., Oncken, O., ... Hase, H. (2012). Toward understanding tectonic control on the Mw 8.8 2010 Maule Chile earthquake. *Earth and Planetary Science Letters*, *321–322*, 152–165. doi: 10.1016/j.epsl.2012.01.006

NCEI, N. C. f. E. (2008). *ETOPO1 1 Arc-Minute Global Relief Model.* https://www.ncei.noaa.gov/access/metadata/landing-page/bin/iso?id=gov.noaa.ngdc.mgg.dem:316.

Obara, K., & Kato, A. (2016). Connecting slow earthquakes to huge earthquakes. *Science*, *353*(6296), 253–257. doi: 10.1126/science.aaf1512

Ortega-Culaciati, F., Simons, M., Ruiz, J., Rivera, L., & Díaz-Salazar, N. (2021). An EPIC Tikhonov Regularization: Application to Quasi-Static Fault Slip Inversion. *Journal of Geophysical Research: Solid Earth*, *126*(7), e2020JB021141. doi: 10.1029/2020JB021141

Ozawa, S., Nishimura, T., Suito, H., Kobayashi, T., Tobita, M., & Imakiire, T. (2011). Coseismic and postseismic slip of the 2011 magnitude-9 Tohoku-Oki earthquake. *Nature*, *475*(7356), 373–6.

Pasyanos, M. E., Masters, T. G., Laske, G., & Ma, Z. (2014). LITHO1.0: An updated crust and lithospheric model of the Earth. *Journal of Geophysical Research: Solid Earth*, *119*(3), 2153–2173. doi: 10.1002/2013JB010626

Peña, C., Heidbach, O., Moreno, M., Bedford, J., Ziegler, M., Tassara, A., & Oncken, O. (2020). Impact of power-law rheology on the viscoelastic relaxation pattern and afterslip distribution following the 2010 Mw 8.8 Maule earthquake. *Earth and Planetary Science Letters*, *542*, 116292. doi: 10.1016/j.epsl.2020.116292

Peña, C., Heidbach, O., Moreno, M., Melnick, D., & Oncken, O. (2021). Transient Deformation and Stress Patterns Induced by the 2010 Maule Earthquake in the Illapel Segment. *Frontiers in Earth Science*, *9*, 157. doi: 10.3389/feart.2021.644834

Pesicek, J. D., Engdahl, E. R., Thurber, C. H., DeShon, H. R., & Lange, D. (2012). Mantle subducting slab structure in the region of the 2010 M8.8 Maule earthquake (30–40S), Chile. *Geophysical Journal International*, *191*(1), 317–324. doi: 10.1111/j.1365-246X.2012.05624.x

Plafker, G., & Savage, J. C. (1970). Mechanism of the Chilean Earthquakes of May 21 and 22, 1960. *GSA Bulletin*, *81*(4), 1001–1030. doi: 10.1130/0016-7606(1970)81[1001:MOTCEO]2.0.CO;2

Pollitz, F. F., Brooks Ben, Tong Xiaopeng, Bevis Michael G., Foster James H., Bürgmann Roland, ... Blanco Mauro (2011). Coseismic slip distribution of the February 27, 2010 Mw 8.8 Maule, Chile earthquake. *Geophysical Research Letters*, *38*(9). doi: 10.1029/2011GL047065

Ragon, T. (2022). *Supplementary Material to: A secondary zone of uplift measured after megathrust earthquakes: Caused by early downdip afterslip?* Zenodo. doi: 10.5281/zenodo.7120837

Ragon, T., & Simons, M. (2021). Accounting for uncertain 3-D elastic structure in fault slip estimates. *Geophysical Journal International*, *224*(2), 1404–1421. doi: 10.1093/gji/ggaa526

Ragon, T., Sladen, A., & Simons, M. (2018). Accounting for uncertain fault geometry in earthquake source inversions – I: Theory and simplified application. *Geophysical Journal International*, *214*(2), 1174–1190. doi: 10.1093/gji/ggy187

Ragon, T., Sladen, A., & Simons, M. (2019). Accounting for uncertain fault geometry in earthquake source inversions – II: Application to the Mw 6.2 Amatrice earthquake, central Italy. *Geophysical Journal International*, *218*(1), 689–707. doi: 10.1093/gji/ggz180

Rietbrock, A., Ryder, I., Hayes, G., Haberland, C., Comte, D., Roecker, S., & Lyon-Caen, H. (2012). Aftershock seismicity of the 2010 Maule Mw=8.8, Chile, earthquake: Correlation between co-seismic slip models and aftershock distribution? *Geophysical Research Letters*, *39*(8). doi: 10.1029/2012GL051308

Rolandone, F., Nocquet, J.-M., Mothes, P. A., Jarrin, P., Vallée, M., Cubas, N., … Font, Y. (2018). Areas prone to slow slip events impede earthquake rupture propagation and promote afterslip. *Science Advances*, *4*(1), eaao6596. doi: 10.1126/sciadv.aao6596

Ruiz, S., & Madariaga, R. (2018). Historical and recent large megathrust earthquakes in Chile. *Tectonophysics*, *733*, 37–56. doi: 10.1016/j.tecto.2018.01.015

Savage, J. C. (1983). A dislocation model of strain accumulation and release at a subduction zone. *Journal of Geophysical Research: Solid Earth*, *88*(B6), 4984–4996. doi: 10.1029/JB088iB06p04984

Tsang, L. L. H., Vergnolle, M., Twardzik, C., Sladen, A., Nocquet, J.-M., Rolandone, F., … Mothes, P. (2019). Imaging rapid early afterslip of the 2016 Pedernales earthquake, Ecuador. *Earth and Planetary Science Letters*, *524*, 115724. doi: 10.1016/j.epsl.2019.115724

van Dinther, Y., Preiswerk, L. E., & Gerya, T. V. (2019). A Secondary Zone of Uplift Due to Megathrust Earthquakes. *Pure and Applied Geophysics*, *176*(9), 4043–4068. doi: 10.1007/s00024-019-02250-z

Vigny, C., Socquet, A., Peyrat, S., Ruegg, J.-C., Métois, M., Madariaga, R., … Kendrick, E. (2011). The 2010 Mw 8.8 Maule Megathrust Earthquake of Central Chile, Monitored by GPS. *Science*, *332*(6036), 1417–1421. doi: 10.1126/science.1204132

Waskom, M. L. (2021). Seaborn: Statistical data visualization. *Journal of Open Source Software*, *6*(60), 3021. doi: 10.21105/joss.03021

Supplementary Material for

A secondary zone of uplift measured after megathrust earthquakes: caused by early downdip afterslip?

Théa Ragon[1*], **Mark Simons** [1]

[1]Seismological Laboratory, California Institute of Technology, Pasadena, CA, USA. , [*]Corresponding author: tragon@caltech.edu

Contents

Bayesian Sampling of the inverse problem 3
- AlTar 3
- Priors and outputs 3

Details for the synthetic case 4
- Mesh properties 4
- True 3D crustal structure, used to calculate the synthetic data 4
- Assumed crustal structures, used for inversion 4
- Additional results 6

Details for the Maule earthquake 11
- Mesh properties 11
- Additional results 13

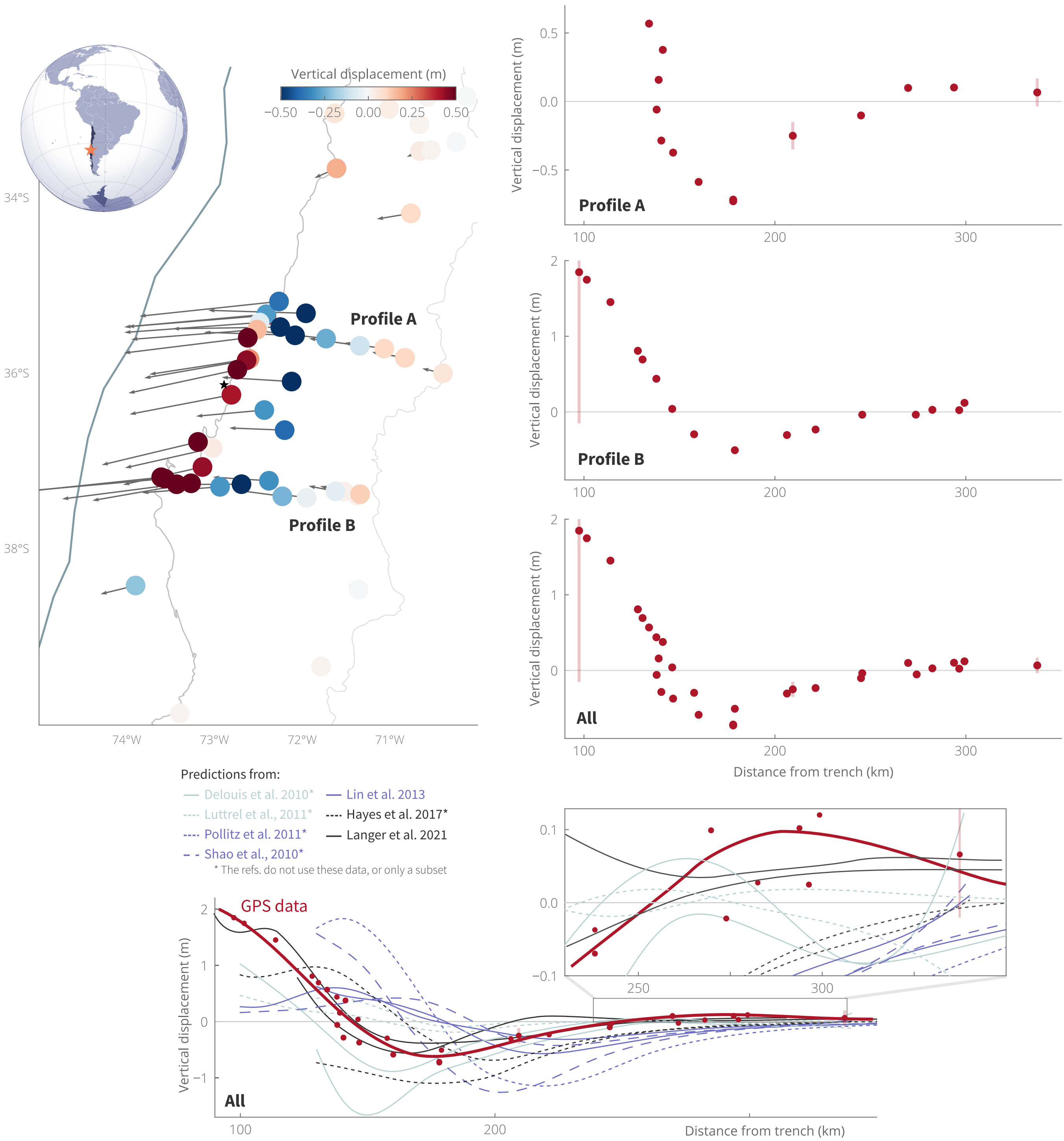

Figure S1 Observed surface displacements in map view and trench-perpendicular profiles of vertical displacements. Vertical bars indicate measurement errors when available.

S1 Bayesian Sampling of the inverse problem

S1.1 AlTar

The sampling is performed with a Bayesian approach implemented in the AlTar2 package, originally formulated by Minson et al. (2013). AlTar combines the Metropolis algorithm with a tempering process to iteratively sample the solution space. A large number of samples are tested in parallel at each transitional step, which is followed by a resampling step, allowing us to select only the most probable models. The probability of each sample to be selected depends on its ability to fit the observations $\mathbf{d}_{\text{obs}}$ within the uncertainties $\mathbf{C}_\chi = \mathbf{C}_{\text{d}} + \mathbf{C}_{\text{p}}$, where $\mathbf{C}_{\text{d}}$ represents the observational errors and $\mathbf{C}_{\text{p}}$ the epistemic uncertainties introduced by approximations of the forward model (e.g. Minson et al., 2013; Duputel et al., 2014; Ragon et al., 2018, 2019).

The solution space is evaluated through repeated updates of the probability density function (PDF) of each sampled parameter

$$p(\mathbf{m}, \beta_i) \propto \; p(\mathbf{m}) \cdot \; exp[-\beta_i \cdot \chi(\mathbf{m})], \tag{1}$$

where $\mathbf{m}$ is the sampled model, $p(\mathbf{m})$ the prior information on this sample, i corresponds to each iteration and β evolves dynamically from 0 to 1 to optimize the parameter space exploration Minson et al. (2013). $\chi(\mathbf{m})$ is the misfit function which quantifies the discrepancies between observations and predictions within uncertainties described by the covariance matrix $\mathbf{C}_\chi$ (Tarantola, 2005; Minson et al., 2013, 2014; Duputel et al., 2014)

$$\chi(\mathbf{m}) = \frac{1}{2}[\mathbf{d}_{\text{obs}} - \mathbf{G}(\mathbf{m})]^T \cdot \mathbf{C}_\chi^{-1} \cdot [\mathbf{d}_{\text{obs}} - \mathbf{G}(\mathbf{m})]. \tag{2}$$

S1.2 Priors and outputs

We solve for both slip amplitude and rake, within the assumed prior distributions specified below.

For the subduction toy model:
- Positive uniform prior $p(\mathbf{m}) = \mathcal{U}(0 \text{ m}, 50 \text{ m})$ for the dip-slip parameters, $p(\mathbf{m}) = \mathcal{N}(0 \text{ m}, 1 \text{ m})$ for the strike-slip parameters.
- Slip is solved at each fault node
- Assumed subfault dimension: 25 km side

For the Maule earthquake:
- Positive uniform prior $p(\mathbf{m}) = \mathcal{U}(0 \text{ m}, 50 \text{ m})$ for the dip-slip parameters, $p(\mathbf{m}) = \mathcal{N}(0 \text{ m}, 2 \text{ m})$ for the strike-slip parameters.
- Slip is solved at each fault node
- Assumed triangular subfault dimension: $\sim$37 km side.

The final output consists in a series of models sampled from among the most plausible models of the full solution space. To explore the results, we consider probabilistic variables, such as a combination of the mean of the sampled models and the associated posterior uncertainty (standard deviation).

S2 Details for the synthetic case

S2.1 Mesh properties

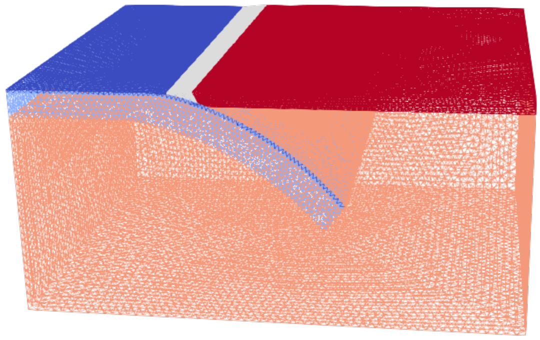

Figure S2 Mesh used to compute the true forward model

- Mesh dimensions: 1250 km x 1000 km x 600 km height
- topography ranges from - 6 km at the trench to 2 km in the volcanic arc
- Elements are tetrahedrons
- Element size increases from 2 km near the fault to 50 km near the edges
- Fault is 500 km long and 200 km wide
- subfaults are triangular

S2.2 True 3D crustal structure, used to calculate the synthetic data

- fault architecture varies along strike
- subfaults dimensions: 5 km side
- Spatially correlated noise is added to synthetic data: 15 km wavelength, 1.5 cm amplitude

Table 1 True 3D elastic properties

Domain	Dimension	Density (kg/m^3)	Vs (m/s)	Vp (m/s)	μ (GPa)	μ/μ_0
oceanic crust	8-km-thick	2800 to 3000	3.5	5.5	34.3 to 50	0.65
wedge	25-km-wide	1900	3.0	5.3	17.0	0.32
slab	12-km-thick	3200	4.5	8	64.8	1.24
continental crust	35-km-thick	2500	4.0	7.0	40	0.76
mantle	-	3000 to 3350	4.2	7.5	52 (μ_0) to 60	1 to 1.15

S2.3 Assumed crustal structures, used for inversion

- Fault architecture is similar to the one adopted for calculating synthetic data, except if indicated otherwise (if planar, the assumed plane is the best fitting one)
- Subfaults dimensions: 25-km-side

Table 2 Layered crust: Assumed elastic properties

Domain	Dimension	Density (kg/m^3)	Vs (m/s)	Vp (m/s)	μ (GPa)	μ/μ_0
oceanic crust	8-km-thick	2800	3.5	5.5	34.3	0.65
mantle	-	3000	4.2	7.5	52 (μ_0)	1.00

Table 3 Assumed (incorrect) 3D crust: elastic properties

Domain	Dimension	Density (kg/m^3)	Vs (m/s)	Vp (m/s)	μ (GPa)	μ/μ_0
oceanic crust	6-km-thick	3000	3.5	5.5	36.75	0.63
wedge	15-km-wide	2400	3.5	6.2	29.4	0.50
slab	16-km-thick	3300	4.5	8.0	66.8	1.15
continental crust	26-km-thick	2700	4.0	7.0	43.2	0.74
mantle	-	3300	4.2	7.5	58 (μ_0)	1

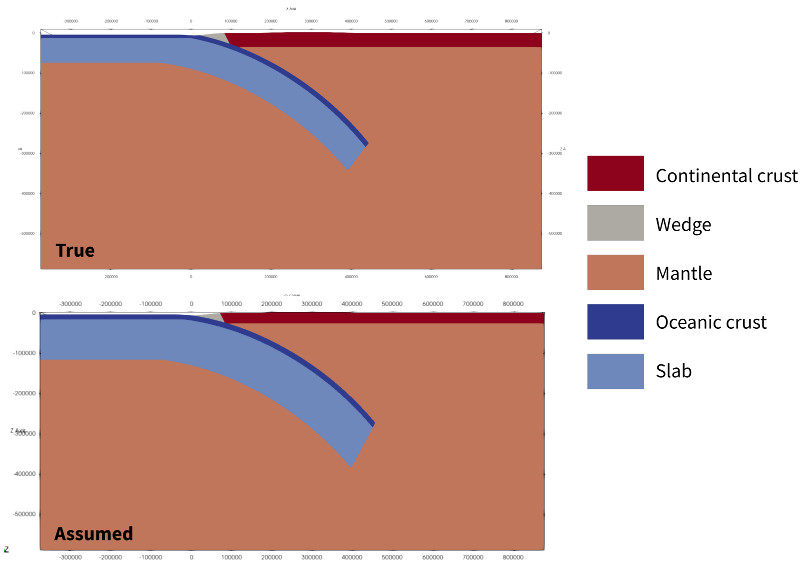

Figure S3 Trench-perpendicular profiles showing the geometries and elastic domains of the crustal structures adopted for calculating synthetic observations (top, true) or for imaging slip (bottom, assumed). Elastic properties for each domain are detailed in Tables 1, 2 and 3.

S2.4 Additional results

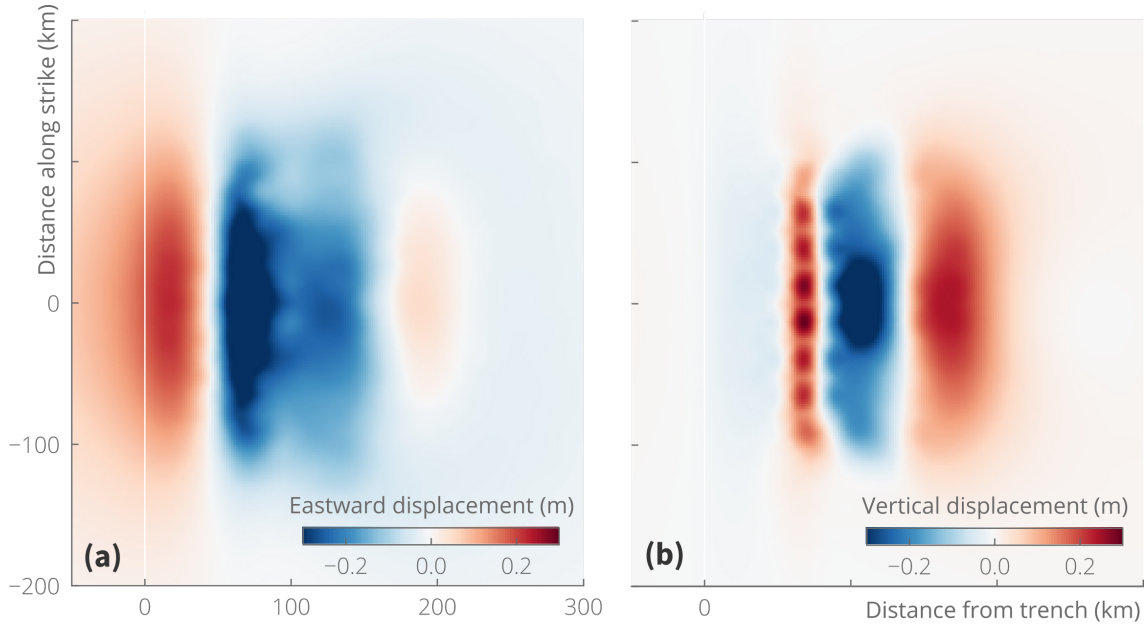

Figure S4 Difference in surface displacements produced by the main slip patch if assuming 3D or layered elastic properties. In (b), the small length-scale rougness is an artefact due to varying spacing of the mesh at this location: it does not impact the results of the inversions as there are no synthetic data in this location. Note that in the far-field (in the primary zone of subsidence, 150-200 km from the trench), the difference in vertical displacement is more than 5 times larger than the difference in horizontal displacement.

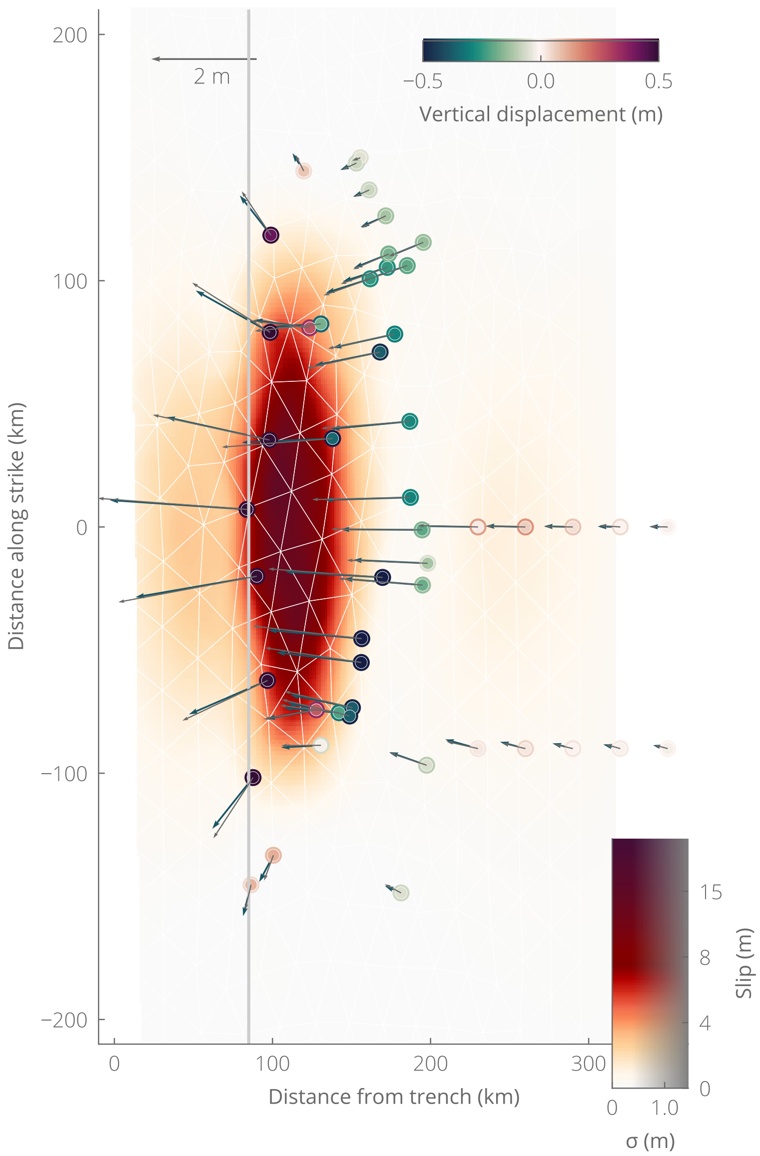

Figure S5 Inferred slip model and predictions assuming the correct fault geometry, an homogeneous crust, and using a simple generalized positive least square approach with very mild spatial smoothing for simplicity. We use the model covariance matrix introduced by Radiguet et al. (2011): $C_m(i,j) = \frac{\sigma\lambda_0}{\lambda}^2 e^{-\frac{||i,j||_2}{\lambda}}$, with σ the amplitude of the correlation, λ the characteristic length scale, and λ_0 a normalizing distance: $\sigma = 2, \lambda = 5$ and $\lambda_0 = 5$.

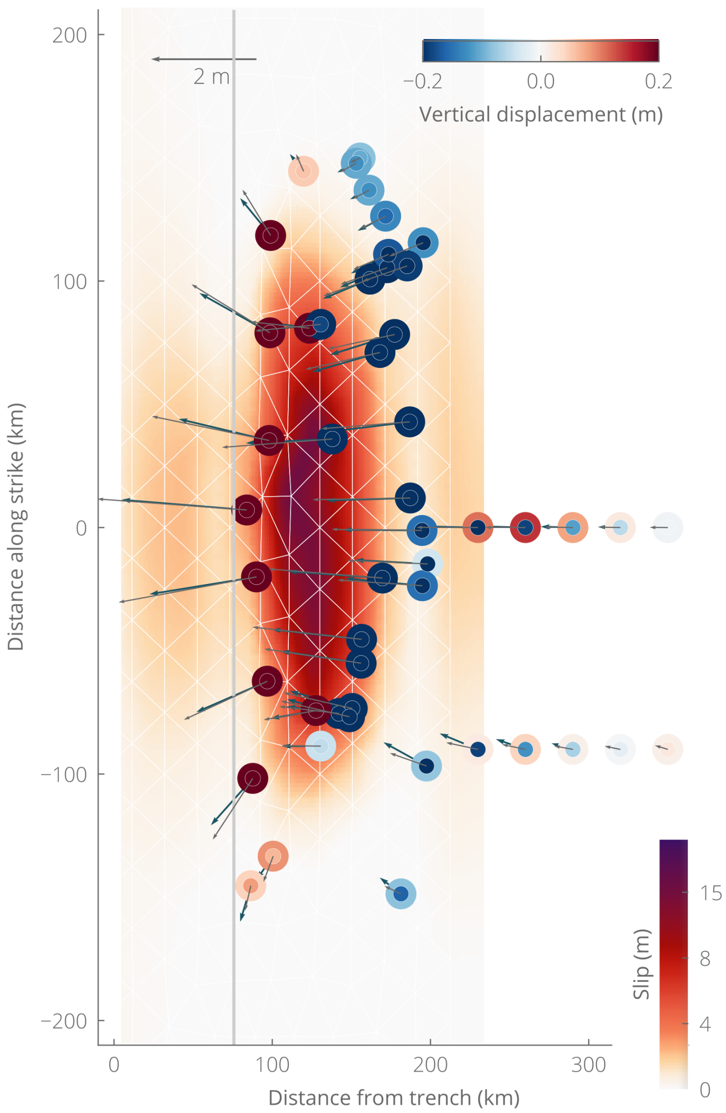

Figure S6 Inferred slip model and predictions assuming a fault extending to a shallower depths, a layered crust, and using a simple generalized positive least square approach with spatial smoothing. We use the model covariance matrix introduced by Radiguet et al. (2011): $C_m(i,j) = \frac{\sigma\lambda_0}{\lambda}^2 e^{-\frac{||i,j||_2}{\lambda}}$, with σ the amplitude of the correlation, λ the characteristic length scale, and λ_0 a normalizing distance: $\sigma = 1$, $\lambda = 8$ and $\lambda_0 = 5$.

$"0- F)! -- .'$+ (* ') +- $ /$*). ..0($)"/# *-- /! 0'/" *(/-4v '
))0)- '$./$ ''4 .('' (.0- ( )/ --*-*) /# 1 -/$ ' / —?uD ((˜ u */ #
1 -/$ ' $.+' ( )/$.* / $) /*/# /-$( )/*!/# !$//*/# #*-$5*)/ '*) u

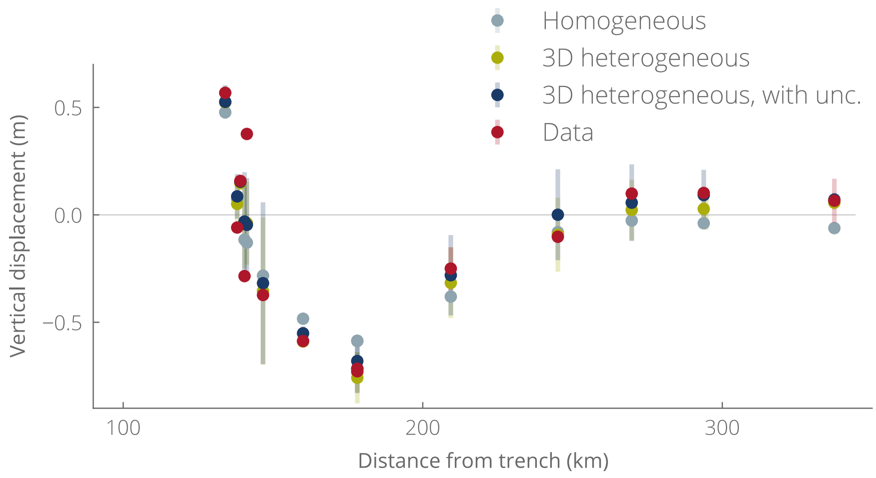

(a) Vertical displacement

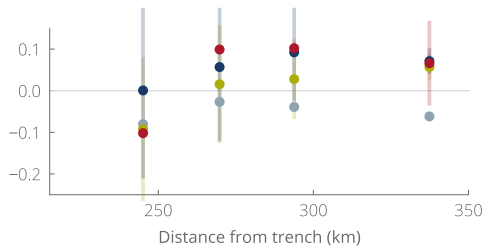

(b) Vertical displacement, zoomed inset

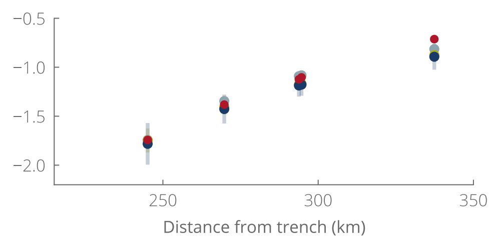

(c) Eastward displacement, zoomed inset

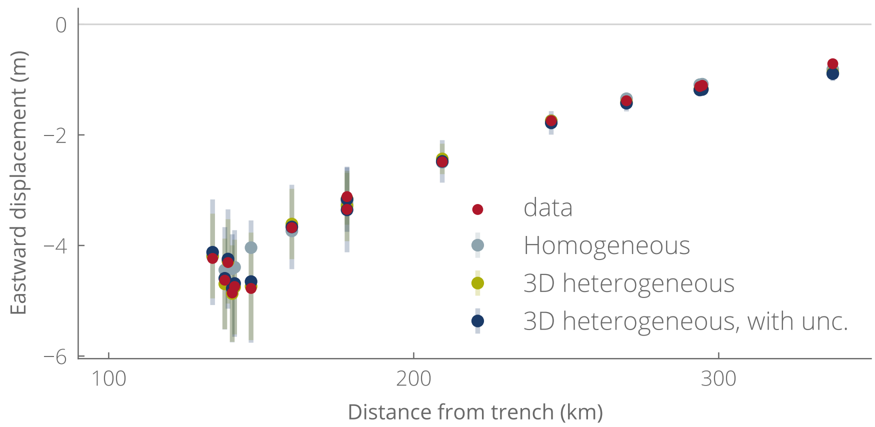

(d) Eastward displacement

Figure S12 Trench perpendicular profile along **profile A** (see Fig. 4) of measured and predicted surface displacements, for the slip models inferred assuming homogeneous or 3D crustal structures, with and without accounting for epistemic uncertainties. Vertical error bars show the posterior uncertainty or data errors.

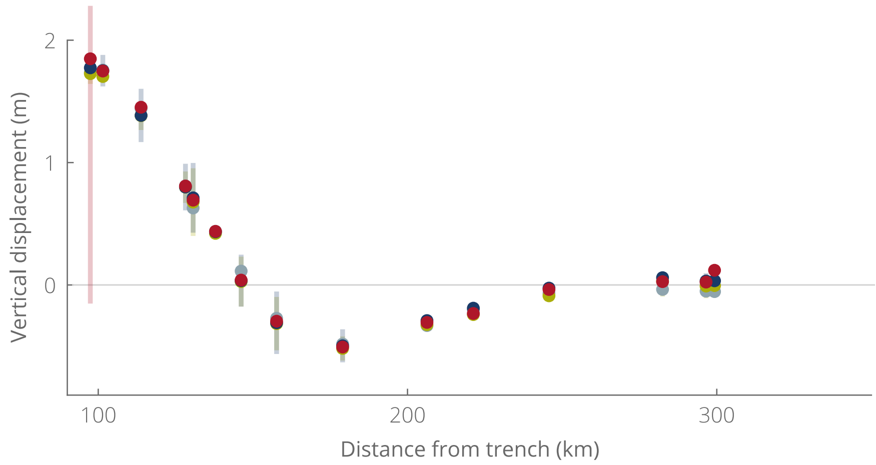

(a) Vertical displacement

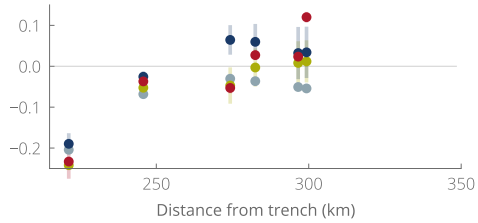

(b) Vertical displacement, zoomed inset

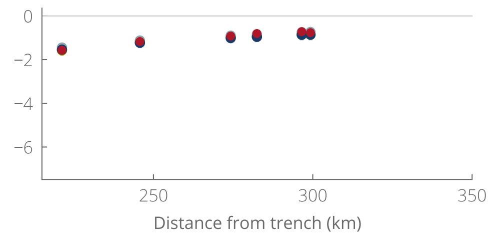

(c) Eastward displacement, zoomed inset

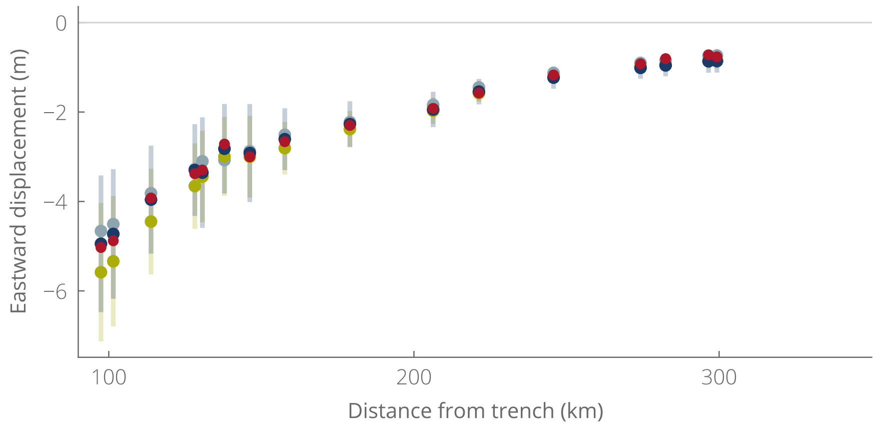

(d) Eastward displacement

Figure S13 Trench perpendicular profile along **profile B** (see Fig. 4) of measured and predicted surface displacements, for the slip models inferred assuming homogeneous or 3D crustal structures, with and without accounting for epistemic uncertainties. Vertical error bars show the posterior uncertainty or data errors. Same colors as in Fig. S12.

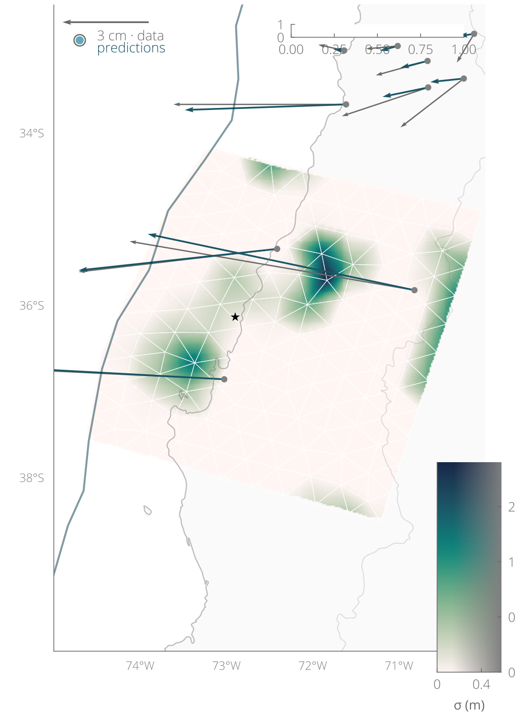

(a) Inferred slip model

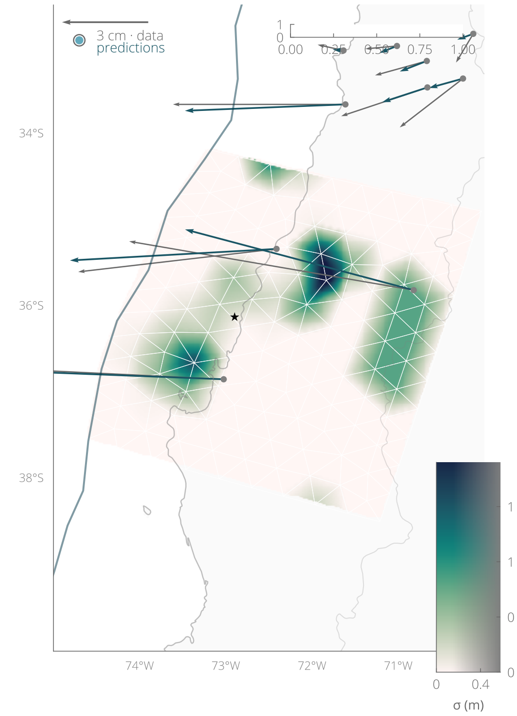

(b) Synthetic slip model with down-dip slip patch

Figure S14 Plausible **12-days afterslip** models for the Maule earthquake. The model in (a) has been inferred with the same assumptions as for the coseismic model. In (b), we modified the slip below 90 km so that it replicates the down-dip slip patch we inferred: this model is also compatible with the data.

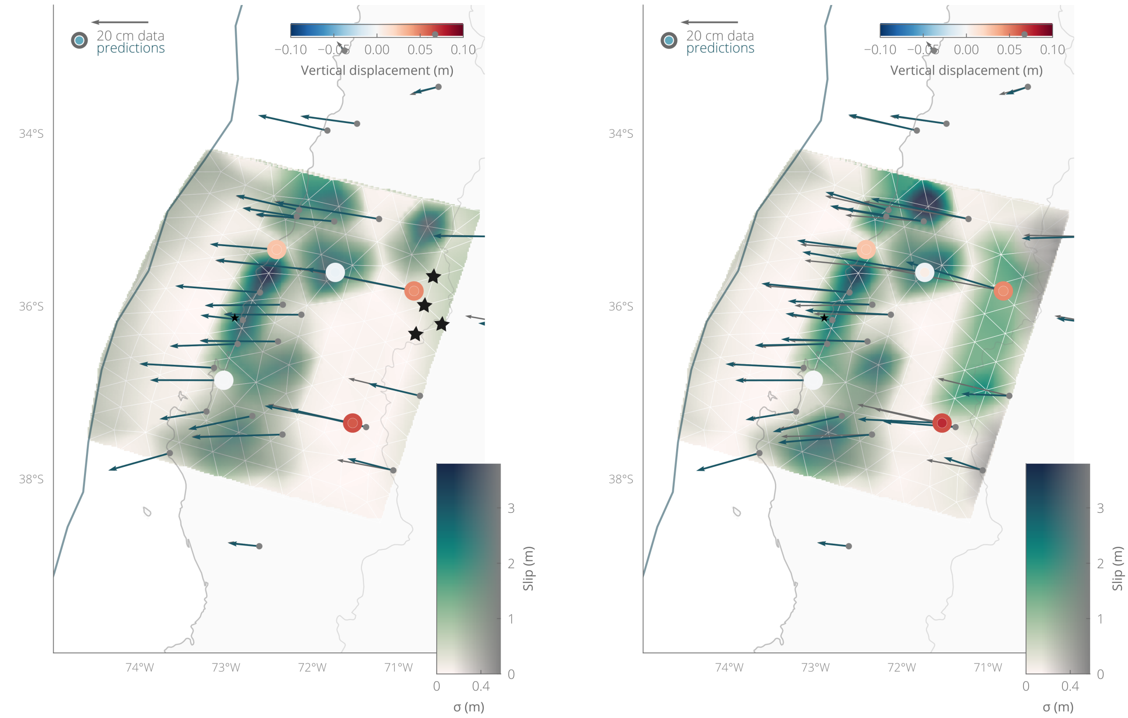

(a) Inferred slip model

(b) Synthetic slip model with down-dip slip patch

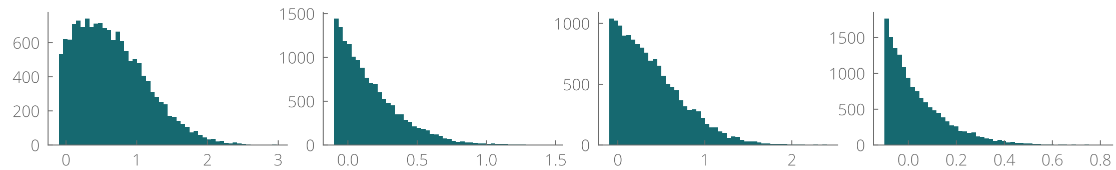

(c) Posterior distribution of potential slip values inferred for model (a) at some locations (black stars, from south to north) within the down-dip patch added in (b)

Figure S15 Plausible $>$**1-year -post-seismic slip** models for the Maule rarthquake. The model in (a) has been inferred with the same assumptions as for the coseismic model. In (b), we modified the slip below 90 km so that it replicates the down-dip slip patch we inferred: this model is also compatible with the data. In (c), the posterior probability density functions of model (a) tell us that the synthetic $\sim$1 m slip of model (b) falls within inferred potential slip values of model (a).

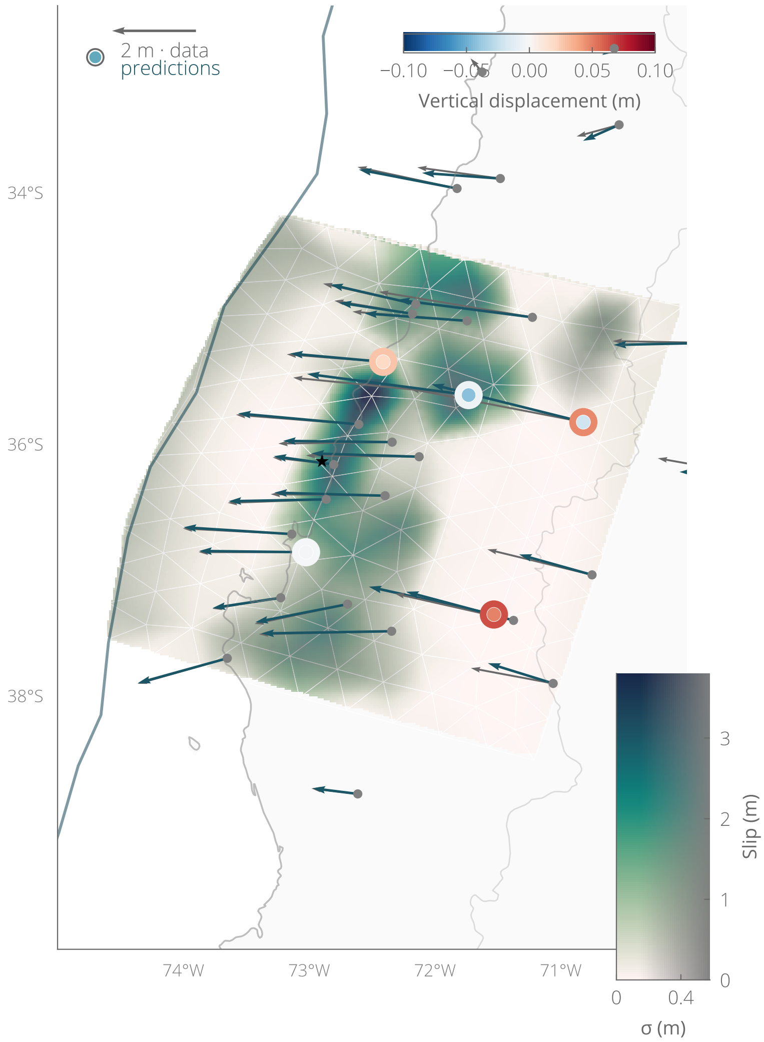

Figure S16 Post-seismic slip model with deep slip removed: deep slip is required to explain the vertical displacement of the distal data.

References

Duputel, Z., Agram, P. S., Simons, M., Minson, S. E., and Beck, J. L. (2014). Accounting for prediction uncertainty when inferring subsurface fault slip. *Geophysical Journal International*, 197(1):464–482. 3

Minson, S. E., Simons, M., and Beck, J. L. (2013). Bayesian inversion for finite fault earthquake source models I – theory and algorithm. *Geophysical Journal International*, 194(3):1701–1726. 3

Minson, S. E., Simons, M., Beck, J. L., Ortega, F., Jiang, J., Owen, S. E., Moore, A. W., Inbal, A., and Sladen, A. (2014). Bayesian inversion for finite fault earthquake source models – II: The 2011 great Tohoku-oki, Japan earthquake. *Geophysical Journal International*, 198(2):922–940. 3

Radiguet, M., Cotton, F., Vergnolle, M., Campillo, M., Valette, B., Kostoglodov, V., and Cotte, N. (2011). Spatial and temporal evolution of a long term slow slip event: The 2006 Guerrero Slow Slip Event. *Geophysical Journal International*, 184(2):816–828. 7, 8

Ragon, T., Sladen, A., and Simons, M. (2018). Accounting for uncertain fault geometry in earthquake source inversions – I: Theory and simplified application. *Geophysical Journal International*, 214(2):1174–1190. 3

Ragon, T., Sladen, A., and Simons, M. (2019). Accounting for uncertain fault geometry in earthquake source inversions – II: Application to the Mw 6.2 Amatrice earthquake, central Italy. *Geophysical Journal International*, 218(1):689–707. 3

Tarantola, A. (2005). *Inverse Problem Theory and Methods for Model Parameter Estimation*. Other Titles in Applied Mathematics. Society for Industrial and Applied Mathematics. 3